
HamQASBench: A Hamiltonian-Informed Diagnostic Benchmark for Evaluating Quantum Architecture Search

Jiayang Niu* School of Computing Technologies RMIT University s4068570@student.rmit.edu.au	Akib Karim* Quantum Systems Data61, CSIRO akib.karim@csiro.au	Yan Wang School of Computing Technologies RMIT University s3646791@student.rmit.edu.au
Jie Li School of Computing Technologies RMIT University hey.jieli@gmail.com	Ke Deng School of Computing Technologies RMIT University ke.deng@rmit.edu.au	Azadeh Alavi School of Computing Technologies RMIT University azadeh.alavi@rmit.edu.au
Muhammad Usman Quantum Systems Data61, CSIRO muhammad.usman@csiro.au	Yongli Ren School of Computing Technologies RMIT University yongli.ren@rmit.edu.au	

Abstract

Quantum Architecture Search (QAS) automates the design of parameterized quantum circuits for variational quantum algorithms, yet existing benchmarks organize instances by molecular identity or qubit count—criteria agnostic to Hamiltonian structure—and rely solely on energy accuracy, which cannot detect structural failures such as over-parameterization on near-product ground states. We introduce HAMQASBENCH, a Hamiltonian-informed diagnostic benchmark organizing 11 molecules into five structural tiers via fingerprints derived from the Pauli operator basis, computational basis representation, and ground-state entanglement. A post-hoc critical-structure extraction procedure identifies minimal circuits consistent with each tier’s requirements, complementing energy-based evaluation with per-qubit entanglement analysis and pairwise state fidelity. Benchmarking five QAS methods across four paradigms reveals failure modes invisible to conventional metrics: over-parameterization in the minimalism regime, eigenstate commitment under degeneracy, a representation bottleneck in strongly correlated systems, topology-induced routing failure, and circuit search space growth as a scalability bottleneck.

1 Introduction

In the noisy intermediate-scale quantum (NISQ) era [1], variational quantum algorithms (VQAs) have emerged as the leading paradigm for near-term quantum computation [2, 3]. Among these, the Variational Quantum Eigensolver (VQE) is particularly prominent for applications in quantum chemistry, where it is used to estimate molecular ground-state energies. Their effectiveness critically depends on the design of the underlying parameterized quantum circuit (PQC), or *ansatz*: a poorly chosen circuit structure lead to barren plateaus, insufficient expressivity, or excessive gate overhead [4, 5]. While fixed ansatz families such as hardware-efficient [6] and problem-inspired [7] templates have been proposed, they often require expert knowledge to construct and may generalize poorly across molecular instances and hardware configurations. These limitations motivate *Quantum Architecture*

*Equal contribution.

Search (QAS) [8–12], which aims to automatically discover circuit structures tailored to a given problem.

A central downstream task of QAS is ground-state energy estimation via VQE [13, 2, 3]: given a molecular qubit Hamiltonian H , find a circuit C minimizing $\langle C(\theta^*)|H|C(\theta^*)\rangle$, where solutions within 1.6 mHa of the true ground-state energy E_0 are said to achieve chemical accuracy [13]. The quality of this estimate is therefore jointly determined by two factors: whether the circuit C is sufficiently expressive to represent the target ground state, and whether the classical optimizer can find suitable parameters θ^* within that circuit. Critically, the structural requirements on C are not uniform across problem instances—they are governed by the properties of the Hamiltonian H itself [14, 15], which vary across molecular systems. For example, a diagonal-dominant Hamiltonian with near-zero ground-state entanglement admits a product-state solution representable by a handful of single-qubit rotations [16, 17], whereas a strongly correlated Hamiltonian with high single-qubit von Neumann entropy [16, 15] demands deep entangling structures spanning the full system. This instance-dependent complexity further underscores the need for automated approaches like QAS to design problem-adaptive circuit architectures. More importantly, existing QAS methods are typically evaluated on molecules organized by identity or qubit count [8–12, 18, 19]—criteria agnostic to these structural properties—and assessed solely on achieved energy, which cannot distinguish a method that learned the right structure from one that prepared a low-lying excited state with similar energy—a structural failure that propagates to downstream calculations such as excited-state spectra [20], dipole moments [21], and thermodynamic properties [22].

Concurrent benchmarking efforts such as BenchRL-QAS [23] and SQuASH [24] have advanced reproducibility and cross-method comparison, but organize molecules by task type or predefined search spaces rather than Hamiltonian structure, and provide no mechanism to assess whether discovered circuits are structurally consistent with the problem’s underlying quantum mechanical requirements. To address these limitations, we introduce HAMQASBENCH, a Hamiltonian-informed diagnostic benchmark for QAS in variational ground-state energy estimation. Rather than selecting molecules by identity or system size, HAMQASBENCH characterizes each molecule through *Hamiltonian structural fingerprints* derived from three complementary views of the qubit Hamiltonian: *Pauli operator basis properties*, *computational basis representation*, and *energy and ground-state correlation structure*. These fingerprints organize an 11-molecule, five-tier diagnostic suite spanning complementary structural regimes: *minimalism*, *degeneracy*, *representation*, *topology*, and *same-family scalability*. The final tier extends to 14-qubit systems via a GPU-accelerated optimization backend (see Section B). To move beyond energy-only evaluation, we introduce a *post-hoc critical-structure extraction* procedure. This procedure iteratively prunes redundant gates from low-error training-stage circuits using counterfactual importance scoring, maintains a beam of candidate circuits under an energy tolerance constraint, and returns a minimal representation whose structure can be directly compared against each tier’s Hamiltonian fingerprints (see Section 3.1). We evaluate five representative QAS methods spanning four major paradigms—reinforcement learning [9, 10], differentiable relaxation [12], training-free filtering [18], and generative modeling [11]—and report cross-method findings invisible to conventional energy-only evaluation.

Our main contributions are as follows: 1) **A structure-aware benchmark.** HAMQASBENCH organizes QAS evaluation around Hamiltonian structural fingerprints rather than molecular identity, enabling principled diagnosis of algorithmic behavior across complementary structural regimes. Molecule generation scripts, evaluation code, and extracted circuit data are publicly available at <https://anonymous.4open.science/r/PSQASBench-D3D7>. 2) **A structural evaluation layer.** The proposed post-hoc critical-structure extraction procedure identifies minimal circuit representations from training-stage circuits, providing a diagnostic signal orthogonal to energy accuracy. For non-degenerate instances, per-qubit von Neumann entropy comparison between pruned circuits and the exact ground state directly quantifies entanglement structure fidelity; for degenerate instances, pairwise state fidelity analysis reveals eigenstate commitment patterns invisible to energy metrics. 3) **Cross-method diagnostic findings.** Benchmarking five methods across four paradigms reveals qualitatively distinct failure modes—including over-parameterization, eigenstate commitment, entanglement mismatch, and topology-induced routing failure—demonstrating that energy accuracy alone is insufficient for diagnosing whether a QAS method has discovered a structurally appropriate circuit.

2 Related Work

Quantum Architecture Search. QAS encompasses a broad range of methods for automatically discovering parameterized quantum circuit structures. Among the most studied, *reinforcement learning* approaches treat circuit construction as a sequential decision process: Ostaszewski et al. [19] pioneered curriculum-based RL for ansatz search, Patel et al. [9] extended this with structured state encodings and dynamic action masking, and Kundu and Mangini [25] improved scalability via tensor-network warm-starting. Niu et al. [10] proposed HyRLQAS, jointly optimizing gate placement and parameter initialization under a hybrid discrete–continuous action space. *Differentiable* methods relax discrete gate selection into a continuous optimization problem [8, 12]. *Sampling-based* methods explore the circuit space by different mechanisms: supernet weight sharing over circuit subarchitectures [26], Monte Carlo tree search over gate sequences [27], and training-free proxy filtering over sampled candidate circuits [18]. *Generative* methods [11, 28] learn autoregressive models over gate sequences. Recent work has also explored block- and gadget-based search spaces [29, 30]. Despite this diversity, existing methods are evaluated on molecules organized by identity or qubit count and primarily on energy accuracy, leaving structural consistency with the underlying Hamiltonian unexamined.

Benchmarking QAS and Neural Architecture Search (NAS). Early QAS benchmarking efforts focused on standardizing problem formulations: Lu et al. [31] proposed a benchmark based on randomly generated unitary targets, Ikhtiarudin et al. [23] systematically evaluated nine RL algorithms across multiple VQA tasks, and Martyniuk et al. [24] leveraged surrogate models to accelerate evaluation across predefined search spaces. Inspired by the rapid growth of benchmarking in the classical NAS community—where tabular and surrogate benchmarks now cover diverse tasks and search spaces [32–35]—the QAS community has similarly recognized the need for principled evaluation. However, existing QAS benchmarks organize instances by task type, system size, or randomly generated targets, and primarily rely on energy-based metrics without probing structural consistency with the underlying Hamiltonian. HAMQASBENCH fills this gap by grounding benchmark construction in Hamiltonian structural properties and introducing a structural evaluation layer orthogonal to energy accuracy.

Hamiltonian Structure and Ansatz Design. The absence of structure-aware benchmarking is particularly striking given that several lines of work have established how Hamiltonian structure should inform ansatz design. From the *Pauli operator basis* perspective, Wiersema et al. [14] showed that the Hamiltonian Variational Ansatz, whose structure mirrors the Hamiltonian’s interaction terms, exhibits superior optimization properties. From the *computational basis* perspective, diagonal dominance governs ground-state proximity to a product state. By the Gershgorin circle theorem [36], strongly diagonal-dominant Hamiltonians confine eigenvalues near the diagonal entries; since computational basis states are product states, a ground state dominated by a single diagonal entry is well approximated by a product state, requiring only shallow circuits to represent [16]. Conversely, Leone et al. [17] established that circuits failing to respect the entanglement structure implied by the Hamiltonian exhibit trainability issues. From the *ground-state entanglement* perspective, Joch et al. [15] showed that ansatz construction guided by von Neumann entropy improves VQE performance, and Woitzik et al. [16] showed that entanglement mismatch impedes convergence. Together, these results establish Hamiltonian structural properties as principled predictors of circuit requirements, directly motivating the fingerprint design of HAMQASBENCH.

3 Hamiltonian-Informed Diagnostic Benchmark

Existing empirical studies in QAS for variational ground-state energy estimation organize molecular instances by identity, qubit count, or conventional chemistry examples [8–12, 18, 19]—criteria agnostic to the structural properties of the underlying Hamiltonian. We instead construct HAMQASBENCH around a set of *Hamiltonian structural fingerprints*, analyzing each molecule’s qubit Hamiltonian from three complementary perspectives: its Pauli operator basis structure, its computational basis representation, and the energy and correlation structure of its ground state.

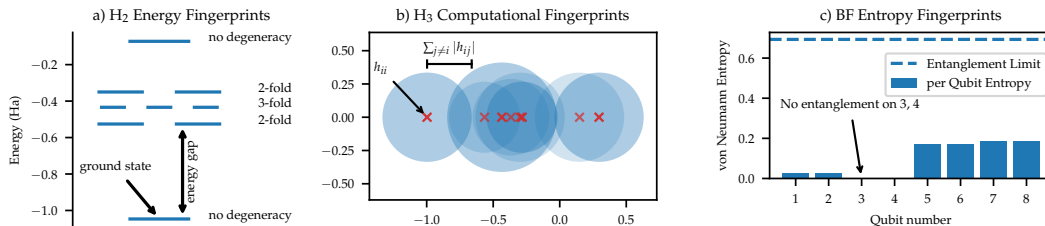


Figure 1: Visual illustration of Hamiltonian structural fingerprints for various molecules.

3.1 Hamiltonian Structural Fingerprints

We derive a set of structural fingerprints from the qubit Hamiltonian across three complementary perspectives. The full theory from quantum chemistry principles are given in the Appendix E. These fingerprints are used to organize the benchmark and are reported in Table 1.

Pauli operator basis fingerprints. We consider the Pauli expansion $H = \sum_i c_i P_i$, where P_i are Pauli strings and c_i are their coefficients. This representation exposes operator composition and interaction structure: Z -only terms are diagonal, while X/Y terms are off-diagonal, inducing basis transitions and entanglement. From this view, we extract two indicators:

$$r_Z = \frac{\sum_{P_i \in Z\text{-only}} |c_i|}{\sum_i |c_i|}, \quad r_{\geq 2} = \frac{\sum_{|P_i| \geq 2} |c_i|}{\sum_i |c_i|}. \quad (1)$$

Here, r_Z measures proximity to a diagonal form, while $r_{\geq 2}$ quantifies the weight carried by multi-qubit interaction terms—equivalently, $r_{\geq 2} = 1 - r_{1\text{-body}}$, the complement of the single-qubit contribution.

Computational basis representation fingerprints. We analyze the Hamiltonian in the computational basis, $H = [h_{ij}]$, to capture diagonal dominance. Let $R_i = \sum_{j \neq i} |h_{ij}|$. We define

$$G_1 = \frac{1}{\dim(H)} \sum_i \mathbf{1}(|h_{ii}| \geq R_i), \quad G_2 = \min_{R_i > 0} \frac{|h_{ii}|}{R_i}. \quad (2)$$

Here, G_1 measures the fraction of diagonally dominant rows, while G_2 captures the weakest diagonal dominance. This is illustrated in Fig. 1 b) as Gershgorin circles with centres h_{ii} and radius R_i .

Energy and ground-state correlation fingerprints. We characterize the spectral and correlation structure of the ground state through three quantities. The excitation gap $\text{Gap} = E_1 - E_0$ measures spectral separation between the ground state and the first excited state; when the ground state is degenerate, $\text{Gap} = 0$, and we explicitly annotate the degeneracy level (e.g., 2-fold or 3-fold) in Table 1 and Fig. 1a). The single-qubit von Neumann entropy [37–39]

$$S(q) = -\text{Tr}(\rho_q \log_2 \rho_q), \quad \rho_q = \text{Tr}_{\bar{q}}(|\psi_0\rangle\langle\psi_0|), \quad (3)$$

where ρ_q is the reduced density matrix of qubit q obtained from the exact ground state $|\psi_0\rangle$, measures how entanglement is distributed across qubits and indicates the representation complexity of the target state. A value of 0 means the qubit is separable as shown in Fig. 1 c), with max value $\ln(2)$.

Together, these fingerprints summarize three complementary perspectives on each instance: Pauli operator basis structure ($r_Z, r_{\geq 2}$), computational basis diagonal dominance (G_1, G_2), and energy and ground-state correlation structure (Gap , degeneracy, $S(q)$).

3.2 Diagnostic Tier Construction

Building on these Hamiltonian structural fingerprints, we construct a 5-tier diagnostic suite (Table 1) through a combination of structure-driven grouping and instance selection. The selected molecules are curated to represent distinct structural regimes, and the resulting tiers are designed to probe complementary and largely orthogonal diagnostic pressures on QAS algorithms.

Table 1: Hamiltonian structural fingerprints for the 11-molecule, 5-tier diagnostic suite in HAMQAS-BENCH. Degenerate ground states are indicated by Gap = 0 with multiplicity (e.g., 2-fold, 3-fold).

Tier	Molecule	q	r_Z	$r_{\geq 2}$	G_1	G_2	Gap (mHa)	$S(q)$
Tier1	BeH2_STO3G	6	0.978	0.593	0.969	0.094	212	[.008,.008,.005,.005,.005,.005]
Tier1	LiH_Equil	6	0.876	0.654	0.891	0.225	77	[.018,.018,.006,.006,.013,.013]
Tier2	CH2	8	0.907	0.483	0.945	0.21	0 (3-fold)	[.004,.004,.004,.070,.000,.000,.000,.068]
Tier3	H2_Stretch	4	0.728	0.849	0.75	0.18	4	[.974,.974,.974,.974]
Tier3	H2O_StrongCorr	8	0.723	0.887	0.648	0.074	94	[.021,.021,.342,.342,.316,.316,.071,.071]
Tier3	H4_Chain	8	0.599	0.809	0.418	0.011	233	[.124,.124,.274,.274,.284,.284,.109,.109]
Tier4	H3_Linear	6	0.709	0.765	0.656	0.021	0 (2-fold)	[.202,.139,.147,.147,.083,.245]
Tier5	BeH2_631G	8	0.953	0.560	0.98	0.046	90	[.024,.024,.002,.002,.002,.002,.021,.021]
Tier5	BeH2_6311G	10	0.923	0.533	0.963	0.01	63	[.011,.011,.001(x4),.008,.008,.002,.002]
Tier5	BeH2_CCPVDZ	12	0.889	0.498	0.904	0.019	68	[.022,.022,.002(x4),.012,.012,.003,.003,.008,.008]
Tier5	BeH2_CCPVDZ	14	0.767	0.700	0.621	0	61	[.039,.039,.023,.023,.014(x4),.018,.018,.009,.009,.016,.016]

Tier 1: Minimalism. Tier 1 targets strongly diagonal-dominant Hamiltonians (r_Z, G_1, G_2 all high) with near-zero ground-state entanglement, for which product-state circuits are provably sufficient. BeH2_STO3G and LiH_Equil represent this regime, with LiH_Equil offering a slightly harder case due to weaker diagonal dominance. This tier probes whether methods recover minimal structures or introduce unnecessary gates when a shallow solution suffices.

Tier 2: Degeneracy. Tier 2 isolates ground-state degeneracy as a diagnostic factor by selecting CH2, which exhibits three-fold degeneracy (Gap = 0) while remaining structurally simple in all other fingerprints (high r_Z, G_1 , low $S(q)$).² This tier evaluates whether methods converge to consistent circuit structures under non-unique optima, or drift across energetically equivalent solutions.

Tier 3: Representation. Tier 3 targets the strong-correlation regime by selecting molecules with reduced diagonal dominance and high ground-state entanglement $S(q)$. H2_Stretch serves as a tractable calibration case ($G_1 = 0.75$, 4 qubits), while H2O_StrongCorr and H4_Chain ($G_1 = 0.418, r_{\geq 2} = 0.809$) introduce heterogeneous and uniform strong correlation at 8 qubits. This tier probes whether methods can faithfully encode strongly correlated ground states, and whether energy convergence implies correct entanglement structure.

Tier 4: Topology. Tier 4 introduces hardware connectivity constraints by restricting two-qubit gates to nearest neighbours. H3_Linear is selected for its end-concentrated entanglement profile ($S(q_0) = 0.202, S(q_5) = 0.245$), which requires long-range correlations that linear connectivity cannot directly implement. This tier evaluates whether methods can route entanglement effectively under topological constraints, independent of correlation complexity.

Tier 5: Same-family scalability. Tier 5 fixes molecular identity to BeH2 and increases basis set complexity across an 8–14 qubit ladder, so that r_Z decreases from 0.953 to 0.767 and G_1 from 0.980 to 0.621 while ground-state entanglement remains controlled ($S_{\max} \leq 0.039$). This isolates circuit search space growth as the sole variable, probing scalability independent of correlation complexity.

The resulting suite covers five complementary structural regimes, as summarized in Table 1. Detailed molecular information is provided in Appendix D.

3.3 Post-hoc Critical-Structure Analysis

Energy alone is insufficient to determine whether a QAS method has learned circuit structures consistent with the Hamiltonian fingerprints. We therefore introduce a critical-structure extraction procedure that prunes redundant gates from *training-stage* circuits while preserving energy performance, isolating the minimal structure implied by each instance. Formally, we consider a set of snapshots

$$\mathcal{S} = \{(C_i, \theta_i, \varepsilon(C_i, \theta_i))\}_{i=1}^N,$$

²<https://pennylane.ai/blog/2024/01/top-20-molecules-for-quantum-computing>

where all circuits correspond to the same molecule and lie within a selected energy-error range. For each snapshot $(C_i, \theta_i, \varepsilon_i) \in \mathcal{S}$, we apply the following pruning procedure.

Gate importance. For a circuit C , we first re-optimize its parameters to obtain $\varepsilon(C)$, and evaluate the counterfactual importance of each gate $g_j \in C$ by

$$\Delta_e(j) = \varepsilon(C \setminus g_j) - \varepsilon(C),$$

which measures the performance degradation caused by removing g_j .

Multi-branch pruning. Instead of greedily removing the least important gate, we construct a sampling distribution inversely weighted by $\Delta_e(j)$, where gates with smaller $\Delta_e(j)$ are more likely to be removed. Starting from the original circuit, we iteratively expand a beam of candidate circuits by removing one gate at a time, while enforcing an energy tolerance constraint $\varepsilon_{\text{allow}}$.

Let \mathcal{B}_t denote the set of candidate circuits at iteration t . For each $C \in \mathcal{B}_t$, we generate candidates by removing one gate, i.e.,

$$\mathcal{N}(C) = \{C \setminus g_j \mid g_j \in C, \varepsilon(C \setminus g_j) \leq \varepsilon_{\text{allow}}\},$$

and construct the next set as

$$\mathcal{B}_{t+1} = \text{TopK}\left(\bigcup_{C \in \mathcal{B}_t} \mathcal{N}(C)\right),$$

where $\text{TopK}(\cdot)$, i.e., a beam of fixed width, retains a fixed number of candidates with the smallest circuit size. This multi-branch exploration is necessary because gate contributions are not independent: removing one gate can change the importance of others due to parameter re-optimization and circuit-level coupling. The procedure iteratively expands candidate circuits and returns the smallest circuit that satisfies the error constraint, whose gate structure can be directly compared against each tier’s Hamiltonian fingerprints. Implementation details are provided in Appendix F.

Structural consistency metrics. Beyond energy, we assess structural consistency through two complementary metrics. For non-degenerate instances, we compute the per-qubit von Neumann entropy of each pruned circuit’s output state and compare it against the exact ground state:

$$\text{MAE}_S = \frac{1}{n} \sum_{q=1}^n |S_{\text{circuit}}(q) - S_{\text{exact}}(q)|,$$

where $S_{\text{circuit}}(q)$ is obtained from the statevector of the re-optimized pruned circuit. A low MAE_S indicates that the circuit faithfully reproduces the ground-state entanglement structure, not merely its energy. For degenerate instances, where the ground-state eigenspace contains multiple orthogonal states, we perform pairwise state fidelity analysis:

$$F_{ij} = |\langle \psi_i | \psi_j \rangle|^2,$$

clustering pruned circuits by fidelity threshold to identify which degenerate eigenstate each circuit targets, revealing eigenstate commitment patterns invisible to energy metrics.

4 Experimental Setup

4.1 Methods and Gate-Space Standardization

To systematically diagnose how different formulations of quantum architecture search behave in HAMQASBENCH, we evaluate five representative methods spanning four major QAS paradigms: reinforcement learning [9, 10], differentiable optimization [12], sampling-based search [18], and generative modeling [11]. Rather than exhaustively covering the QAS literature, we select methods that capture distinct search mechanisms: sequential policy learning (CRLQAS, HYRLQAS), continuous architecture relaxation (QUANTUMDARTS), proxy-guided candidate filtering (TFQAS), and autoregressive circuit generation (GQEQAS).

To ensure that performance differences arise from search strategies rather than representational mismatches, we standardize the gate basis across all methods to $\{\text{RX}, \text{RY}, \text{RZ}, \text{CNOT}\}$ while preserving each method’s native search mechanism. Table 2 summarizes the original gate pool, the pool used during benchmark search, the evaluation basis, and the stage at which each adaptation is applied. Detailed implementation choices are provided in Appendix A.

Table 2: Gate-pool standardization and evaluation-basis alignment.

Method	Original paper pool	Benchmark search pool	Eval. basis	Adaptation stage
CRLQAS	{RX, RY, RZ, CNOT}	Same	Same	None
HYRLQAS	{RX, RY, RZ, CNOT}	Same	Same	None
QUANTUMDARTS	{Rz-Ry-Rz, I, CNOT}	Same	{RX, RY, RZ, CNOT}	Eval-time lowering
TFQAS	{RX, RY, RZ, XX, YY, ZZ}	{RX, RY, RZ, CNOT}	{RX, RY, RZ, CNOT}	Search-time replacement
GQEQAS	operator-pool-based	discretized gate-token pool	{RX, RY, RZ, CNOT}	Search-time replacement

4.2 Benchmark Configuration and Evaluation Protocol

Local optimizer and acceleration. Circuit optimization is the primary bottleneck for scaling HAMQASBENCH to larger systems, as training QAS models beyond 10 qubits requires repeated quantum-state simulation at each optimization step. We develop a GPU-enabled *Optimizer Parallelization and Execution Backend* that exploits batched circuit evaluation and parallel optimizer execution to accelerate parameter optimization. Under this backend, COBYLA [40] is used for systems up to 6 qubits for its robustness, while Rotosolve [41] is employed for larger systems due to its batched coordinate-sweep structure that enables efficient GPU acceleration. This configuration is critical for scaling the benchmark to the 10q–14q regime. Further details and empirical efficiency gains are provided in Appendix B.

Circuit budget and connectivity variants. For the Tier 1 molecule BeH2_STO3G and LiH_Equil, we evaluate under two maximum circuit depth budgets: *Shallow* (depth ≤ 10) and *Deep* (depth ≤ 50). This pair tests whether a method discovers a compact solution or overfills the available budget, which is the central diagnostic pressure of Tier 1. For Tier 4 (H3_Linear), we evaluate under two connectivity settings: *All* (all-to-all two-qubit gates permitted) and *Linear* (nearest-neighbour only, 1D chain topology). This isolates the additional difficulty introduced by hardware connectivity constraints, independent of the representational challenge of the underlying Hamiltonian.

Evaluation protocol. For learning-based methods (RL, differentiable, and generative QAS), we perform periodic evaluation by sampling multiple circuits from the current model during training, providing a stable estimate of search quality while reducing variance from stochastic circuit sampling. TFQAS, which is training-free, directly produces a ranked set of candidate circuits on which evaluation is applied after final parameter optimization. For all methods, we report the best circuit found across the evaluation window, measured by energy error and CNOT count, ensuring a consistent comparison criterion across all QAS paradigms. Hyperparameters, training budgets, and the number of sampled circuits per evaluation are provided in Appendix C.

5 Main Benchmark Results

Tables 3 and 4 report the best circuits obtained across evaluation checkpoints for each method–molecule pair, measured by energy error (mHa), CNOT count, and rotation-gate count, with chemical accuracy (1.6 mHa) as the success threshold. In parallel, Table 6 reports per-qubit von Neumann entropy consistency (MAE_S) between pruned circuits and exact ground states for Tier 1 and Tier 3, providing a structural diagnostic orthogonal to energy accuracy. Training-stage best results and full structural analyses are reported in Appendix G.2.

Tier 1: Minimalism. Tier 1 targets diagonal-dominant Hamiltonians with near-zero ground-state entanglement, for which compact product-state circuits are sufficient. Most methods reach chemical accuracy on both BeH2_STO3G and LiH_Equil; LiH_Equil is slightly more demanding due to weaker diagonal dominance. The exception is TFQAS under the deep budget, where training-free proxy filtering loses reliability as the search space expands.

Critical-structure extraction collapses retained circuits to 2-gate structures across methods (Fig. 2), and per-qubit entropy analysis confirms structural consistency: $MAE_S \leq 0.012$ for both molecules (Table 6), with pruned circuits correctly reproducing the near-product entanglement structure ($\bar{S}_{\text{exact}} \leq 0.012$) using rotation-only gates. However, the redundancy analysis in Table 5 reveals that methods achieving identical energy differ substantially in structural efficiency—from 6.7% redun-

Table 3: Best Evaluation-stage QAS results on the T1–T4 diagnostic tiers of HAMQASBENCH.

Molecule	T1_BeH2_6q (Shallow)			T1_BeH2_6q (Depth)			T1_LiH_Equil_6q (Shallow)			T1_LiH_Equil_6q (Depth)			T2_CH2_8q		
	Error	Cnot	Rot	Error	Cnot	Rot	Error	Cnot	Rot	Error	Cnot	Rot	Error	Cnot	Rot
CRLQAS	5.54E-04	0	3	5.54E-04	2	3	1.05E-03	6	4	1.05E-03	2	3	3.57E-07	21	15
HyRLQAS	5.54E-04	0	2	5.54E-04	0	2	1.05E-03	0	2	1.05E-03	0	2	4.48E-04	14	13
QuantumDARTS	5.54E-04	11	6	5.54E-04	14	9	1.05E-03	3	3	1.05E-03	3	3	5.66E-03	66	12
GQEQAS	5.54E-04	0	6	5.55E-04	13	6	1.05E-03	0	4	1.05E-03	4	19	4.18E-02	1	30
TFQAS	5.54E-04	5	4	1.89E-02	26	23	1.05E-03	5	4	1.01E-02	26	22	3.69E-01	35	26

Molecule	T3_H2_Stretch_4q			T3_H2O_StrongCorr_8q			T3_H4_Chain_8q			T4_H3_Linear_6q_All			T4_H3_Linear_6q_Linear		
	Error	Cnot	Rot	Error	Cnot	Rot	Error	Cnot	Rot	Error	Cnot	Rot	Error	Cnot	Rot
CRLQAS	3.39E-10	5	4	4.67E-02	41	29	6.78E-02	47	23	2.42E-02	36	34	2.46E-02	17	53
HyRLQAS	8.57E-11	8	7	6.58E-02	48	22	6.78E-02	9	62	4.64E-02	33	17	4.64E-02	8	12
QuantumDARTS	2.44E-03	24	12	1.43E-01	13	6	6.78E-02	13	9	4.64E-02	44	9	4.64E-02	19	6
GQEQAS	2.88E-03	16	26	6.13E-01	2	39	2.18E-01	6	25	6.88E-02	7	16	2.11E-01	0	19
TFQAS	4.71E-03	28	19	2.91E-01	37	32	7.80E-01	40	29	1.71E-01	24	24	2.17E-01	24	24

Table 4: Best Evaluation-stage QAS results on the T5 same-family BeH₂ of HAMQASBENCH.

Molecule	T5_BeH2_6q			T5_BeH2_631G_8q			T5_BeH2_6311G_10q			T5_BeH2_CCPVDZ_12q			T5_BeH2_CCPVDZ_14q		
	Error	Cnot	Rot	Error	Cnot	Rot	Error	Cnot	Rot	Error	Cnot	Rot	Error	Cnot	Rot
CRLQAS	5.54E-04	0	3	2.34E-04	13	19	8.97E-04	7	4	2.00E-03	89	11	6.15E-03	56	44
HyRLQAS	5.54E-04	0	2	2.17E-03	58	12	8.97E-04	6	21	2.00E-03	89	11	1.58E-01	81	19
QuantumDARTS	5.54E-01	11	6	2.17E-03	1	6	8.97E-04	1	6	2.60E-01	19	3	3.01E-01	14	12
GQEQAS	5.54E-04	0	6	2.82E-02	0	31	2.80E-01	40	40	2.00E-03	39	61	7.21E-01	22	36
TFQAS	5.54E-04	5	4	2.07E-01	36	31	3.83E-01	51	41	1.45E-01	50	29	3.26E-01	45	22

dancy (HYRLQAS, shallow) to 93.8%(QUANTUMDARTS)—a difference invisible to energy-only evaluation.

Tier 2: Degeneracy. Tier 2 evaluates QAS behavior under degenerate Hamiltonians, where multiple distinct circuits achieve equivalent ground-state energy. On CH2 (3-fold degenerate, Gap = 0), methods fail for qualitatively distinct algorithmic reasons. CRLQAS discovers chemical-accuracy solutions frequently during training, but fidelity analysis reveals an *eigenstate commitment* phenomenon: as the DQN converges to compact CNOT skeletons, each seed preferentially locks onto one orthogonal eigenstate (cross-cluster fidelity = 0), with different seeds committing to different eigenstates. This commitment is not absolute—early exploration produces circuits from both eigenstates—but becomes dominant mid-training and persists, causing the greedy eval policy to fail consistently (5–10% success rate). As illustrated in Fig. 2, critical-structure extraction identifies two structurally distinct minimal circuits: Degenerate Structure A entangles q_6 and q_4 via q_0 , while Structure B entangles q_3 and q_5 via a different CNOT topology—both achieve identical energy yet represent orthogonal quantum states. HyRLQAS fails differently via REINFORCE policy collapse under high gradient variance, while GQEQAS cannot generalize from sparse reward signal. QUANTUMDARTS and TFQAS find no chemical-accuracy solutions, as continuous relaxation and proxy filtering both lose discriminative signal in the flat degenerate energy landscape. Across all methods, identical energies mask orthogonal quantum states—a failure mode invisible to energy-only evaluation.

Tier 3: Representation. Tier 3 evaluates whether QAS methods can represent strongly correlated ground states. A clear transition is observed: RL-based methods achieve near-exact solutions on H2_Stretch, while all methods fail to reach chemical accuracy on the larger instances H2O_StrongCorr and H4_Chain.

Per-qubit entropy analysis (Table 6) sharpens this picture. On H2_Stretch, despite near-maximal ground-state entanglement ($S_{\text{exact}} = 0.974$), pruned circuits achieve $\text{MAE}_S = 0.000$, confirming that methods are not biased toward product states and can faithfully encode strong correlation when the Hilbert space is small. On H2O_StrongCorr, even when energy has not fully converged ($\varepsilon \approx 4.6$ mHa), pruned circuits capture the dominant entanglement on q_2 – q_7 ($\text{MAE}_S = 0.028$) while missing the weaker correlations on q_0 and q_1 , suggesting that structural failure precedes energy failure. On H4_Chain under all-to-all connectivity, $\text{MAE}_S = 0.068$ with boundary qubits q_1 and q_6 showing zero captured entanglement, confirming that representation failure is structural rather than parametric. The effect of linear connectivity on H4_Chain is analyzed in Appendix G.3, where

Table 5: Gate redundancy rates of chemical-accuracy circuits on BeH2_ST03G relative to the 2-gate minimal structure. Full statistics are provided in Appendix G.2.

	HYRLQAS	CRLQAS	GQEAS	TFQAS	QuantumDARTS
Shallow	6.7%	66.1%	74.7%	79.7%	94.8%
Deep	25.3%	80.2%	85.2%	—	93.8%

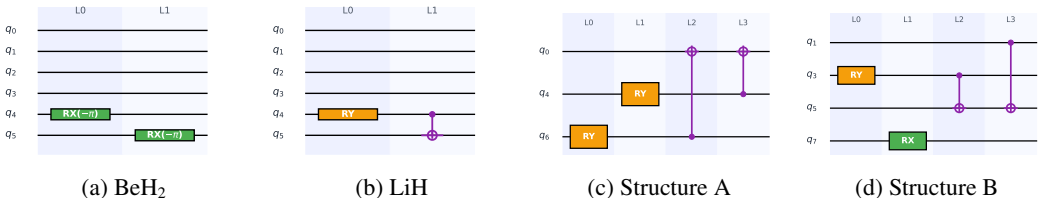


Figure 2: Critical-structure analysis. (a,b) Tier 1 circuits collapse to 2-gate minimal forms. (c,d) Tier 2 yields two structurally distinct circuits targeting orthogonal degenerate eigenstates of CH2.

MAE_S rises to 0.121 and four boundary qubits lose all captured entanglement—demonstrating that energy and entanglement structure can decouple under connectivity constraints.

Tier 4: Topology. Tier 4 evaluates whether QAS methods can realize required correlations under hardware connectivity constraints. On H3_Linear (2-fold degenerate, $\text{Gap} = 0$), enforcing nearest-neighbour connectivity causes a clear performance drop relative to all-to-all, with errors increasing by more than an order of magnitude across methods. As the ground-state degeneracy of H3_Linear introduces the same eigenstate ambiguity as Tier 2, MAE_S analysis is not directly applicable; the connectivity effect on entanglement structure is instead isolated on H4_Chain (Appendix G.3). Training-stage critical-structure analysis on H3_Linear reveals the mechanism: under all-to-all connectivity, retained circuits include long-range CNOTs enabling end-to-end information flow, while under linear connectivity, circuits reuse only short-range local interactions, forming local hubs but failing to propagate correlations across the full system. The performance gap is thus not due to optimization failure but to a structural limitation in information routing.

Tier 5: Same-family scalability. Tier 5 evaluates scalability under increasing system size with controlled molecular structure. On the BeH2 basis ladder (8–14 qubits), ground-state entanglement remains uniformly low ($S_{\max} \leq 0.039$) and the spectrum remains gapped throughout, confirming that Hamiltonian complexity is controlled. Despite this, a sharp performance transition is observed: at 10 qubits, RL-based methods achieve high success rates (HYRLQAS 100%, CRLQAS 90%) with compact circuits (HYRLQAS mean 1.0 CNOT), while all other paradigms largely fail; at 12 and 14 qubits, all methods deteriorate to near-zero evaluation success. Per-qubit entropy analysis confirms that the difficulty is not entanglement complexity: at 12 qubits, training circuits faithfully reproduce the exact ground-state entanglement ($MAE_S = 0.005$) yet fail to stabilize, and at 14 qubits, even a structurally sound training circuit cannot be re-optimized reliably—the optimizer itself fails in the 2^{14} -dimensional parameter space. Tier 5 thus reveals two compounding scalability bottlenecks: search policy instability and parameter optimization failure, both independent of Hamiltonian correlation structure. Full results are provided in Appendix G.4.

6 Conclusion

We introduced HAMQASBENCH, which organizes evaluation around Hamiltonian structural fingerprints rather than molecular identity, and complements energy-based metrics with post-hoc critical-structure extraction and per-qubit entanglement analysis. Across five tiers spanning eleven molecules and up to 14 qubits, we find that energy accuracy is an unreliable proxy for structural correctness: methods can achieve chemical accuracy via over-parameterized circuits, commit to orthogonal eigenstates under degeneracy, or encode worse entanglement structure while reaching lower energy under connectivity constraints—failure modes that remain invisible to conventional evaluation. We hope HAMQASBENCH provides a principled foundation for diagnosing and improving QAS methods beyond energy metrics alone.

Table 6: Entanglement structure consistency between CRLQAS pruned circuits and exact ground states, measured by mean per-qubit von Neumann entropy and MAE_S .

Tier	System	n_q	Error (mHa)	\bar{S}_{exact}	\bar{S}_{circuit}	MAE_S
T1	BeH ₂ STO-3G	6	0.55	0.006	0.000	0.006
T1	LiH (equil.)	6	1.05	0.012	0.000	0.012
T3	H ₂ ($R=2.5$ Å)	4	0.00	0.974	0.974	0.000
T3	H ₂ O	8	4.61	0.187	0.157	0.028
T3	H ₄ Chain	8	33.55	0.198	0.130	0.068

Limitations. First, the per-qubit entropy analysis (MAE_S) is based on CRLQAS training-stage circuits, as it produces the largest pool of chemical-accuracy snapshots suitable for pruning. While this provides a principled structural baseline, extending the analysis to other paradigms remains a direction for future work. Second, the ground-state degeneracy of H3_Linear introduces eigenstate ambiguity that precludes direct MAE_S comparison; we address this by isolating the connectivity effect on entanglement structure using H4_Chain (Appendix G.3), where degeneracy is absent.

References

- [1] Kishor Bharti, Alba Cervera-Lierta, Thi Ha Kyaw, Tobias Haug, Sumner Alperin-Lea, Abhinav Anand, Matthias Degroote, Hermanni Heimonen, Jakob S Kottmann, Tim Menke, et al. Noisy intermediate-scale quantum algorithms. *Reviews of Modern Physics*, 94(1):015004, 2022.
- [2] Jarrod R McClean, Jonathan Romero, Ryan Babbush, and Alán Aspuru-Guzik. The theory of variational hybrid quantum-classical algorithms. *New Journal of Physics*, 18(2):023023, 2016.
- [3] Marco Cerezo, Andrew Arrasmith, Ryan Babbush, Simon C Benjamin, Suguru Endo, Keisuke Fujii, Jarrod R McClean, Kosuke Mitarai, Xiao Yuan, Lukasz Cincio, et al. Variational quantum algorithms. *Nature Reviews Physics*, 3(9):625–644, 2021.
- [4] Jarrod R McClean, Sergio Boixo, Vadim N Smelyanskiy, Ryan Babbush, and Hartmut Neven. Barren plateaus in quantum neural network training landscapes. *Nature communications*, 9(1):4812, 2018.
- [5] Yuxuan Du, Min-Hsiu Hsieh, Tongliang Liu, and Dacheng Tao. Expressive power of parametrized quantum circuits. *Physical Review Research*, 2(3):033125, 2020.
- [6] Abhinav Kandala, Antonio Mezzacapo, Kristan Temme, Maika Takita, Markus Brink, Jerry M Chow, and Jay M Gambetta. Hardware-efficient variational quantum eigensolver for small molecules and quantum magnets. *nature*, 549(7671):242–246, 2017.
- [7] Dave Wecker, Matthew B Hastings, and Matthias Troyer. Progress towards practical quantum variational algorithms. *Physical Review A*, 92(4):042303, 2015.
- [8] Shi-Xin Zhang, Chang-Yu Hsieh, Shengyu Zhang, and Hong Yao. Differentiable quantum architecture search. *Quantum Science and Technology*, 7(4):045023, 2022.
- [9] Yash J Patel, Akash Kundu, Mateusz Ostaszewski, Xavier Bonet-Monroig, Vedran Dunjko, and Onur Danaci. Curriculum reinforcement learning for quantum architecture search under hardware errors. In *The Twelfth International Conference on Learning Representations*.
- [10] Jiayang Niu, Yan Wang, Jie Li, Ke Deng, Azadeh Alavi, Muhammad Usman, and Yongli Ren. Hybrid action reinforcement learning for quantum architecture search. *arXiv preprint arXiv:2511.04967*, 2025.
- [11] Kouhei Nakaji, Lasse Bjørn Kristensen, Ryota Kemmoku, Jorge A Campos-Gonzalez-Angulo, Mohammad Ghazi Vakili, Haozhe Huang, Mohsen Bagherimehrab, Christoph Gorgulla, FuTe Wong, Alex McCaskey, et al. The generative quantum eigensolver (gqe) and its application for ground state search. *arXiv preprint arXiv:2401.09253*, 2024.
- [12] Wenjie Wu, Ge Yan, Xudong Lu, Kaisen Pan, and Junchi Yan. Quantumdarts: differentiable quantum architecture search for variational quantum algorithms. In *International conference on machine learning*, pages 37745–37764. PMLR, 2023.
- [13] Alberto Peruzzo, Jarrod McClean, Peter Shadbolt, Man-Hong Yung, Xiao-Qi Zhou, Peter J Love, Alán Aspuru-Guzik, and Jeremy L O’Brien. A variational eigenvalue solver on a photonic quantum processor. *Nature communications*, 5(1):4213, 2014.
- [14] Roeland Wiersema, Cunlu Zhou, Yvette de Sereville, Juan Felipe Carrasquilla, Yong Baek Kim, and Henry Yuen. Exploring entanglement and optimization within the hamiltonian variational ansatz. *PRX quantum*, 1(2):020319, 2020.
- [15] Alina Joch, Götz S Uhrig, and Benedikt Fauseweh. Entanglement-informed construction of variational quantum circuits. *Quantum Science and Technology*, 10(3):035032, 2025.
- [16] Andreas JC Woitzik, Panagiotis Kl Barkoutsos, Filip Wudarski, Andreas Buchleitner, and Ivano Tavernelli. Entanglement production and convergence properties of the variational quantum eigensolver. *Physical Review A*, 102(4):042402, 2020.
- [17] Lorenzo Leone, Salvatore FE Oliviero, Lukasz Cincio, and Marco Cerezo. On the practical usefulness of the hardware efficient ansatz. *Quantum*, 8:1395, 2024.

- [18] Zhimin He, Maijie Deng, Shenggen Zheng, Lvzhou Li, and Haozhen Situ. Training-free quantum architecture search. In *Proceedings of the AAAI conference on artificial intelligence*, volume 38, pages 12430–12438, 2024.
- [19] Mateusz Ostaszewski, Lea M Trenkwalder, Wojciech Masarczyk, Eleanor Scerri, and Vedran Dunjko. Reinforcement learning for optimization of variational quantum circuit architectures. *Advances in neural information processing systems*, 34:18182–18194, 2021.
- [20] Shaobo Zhang, Akib Karim, Harry M. Quiney, and Muhammad Usman. Full band-structure calculation of semiconducting materials on a noisy quantum processor. *Phys. Rev. A*, 110:062415, 2024.
- [21] Michael A. Jones, Harish J. Vallury, Manolo C. Per, Harry M. Quiney, and Lloyd C. L. Hollenberg. Moments-based improved quantum computation of the electric dipole moment of molecular systems. *Phys. Rev. Appl.*, 25:054001, 2026.
- [22] Thomas E. O’Brien, Michael Streif, Nicholas C. Rubin, Raffaele Santagati, Yuan Su, William J. Huggins, Joshua J. Goings, Nikolaj Moll, Elica Kyoseva, Matthias Degroote, Christofer S. Tautermann, Joonho Lee, Dominic W. Berry, Nathan Wiebe, and Ryan Babbush. Efficient quantum computation of molecular forces and other energy gradients. *Phys. Rev. Res.*, 4:043210, 2022.
- [23] Azhar Ikhtiarudin, Aditi Das, Param Thakkar, and Akash Kundu. Benchrl-qas: Benchmarking reinforcement learning algorithms for quantum architecture search. In *Proceedings of the AAAI Symposium Series*, volume 7, pages 358–367, 2025.
- [24] Darya Martyniuk, Johannes Jung, Daniel Barta, and Adrian Paschke. Benchmarking quantum architecture search with surrogate assistance. *arXiv preprint arXiv:2506.06762*, 2025.
- [25] Akash Kundu and Stefano Mangini. Tensorrl-qas: Reinforcement learning with tensor networks for scalable quantum architecture search. *arXiv preprint arXiv:2505.09371*, 2025.
- [26] Ho Lun Tang, VO Shkolnikov, George S Barron, Harper R Grimsley, Nicholas J Mayhall, Edwin Barnes, and Sophia E Economou. qubit-adapt-vqe: An adaptive algorithm for constructing hardware-efficient ansätze on a quantum processor. *PRX Quantum*, 2(2):020310, 2021.
- [27] Peiyong Wang, Muhammad Usman, Udaya Parampalli, Lloyd CL Hollenberg, and Casey R Myers. Automated quantum circuit design with nested monte carlo tree search. *IEEE Transactions on Quantum Engineering*, 4:1–20, 2023.
- [28] Florian Fürtter, Gorka Muñoz-Gil, and Hans J Briegel. Quantum circuit synthesis with diffusion models. *Nature Machine Intelligence*, 6(5):515–524, 2024.
- [29] Jan Olle, Oleg M Yevtushenko, and Florian Marquardt. Scaling the automated discovery of quantum circuits via reinforcement learning with gadgets. *arXiv preprint arXiv:2503.11638*, 2025.
- [30] Akash Kundu and Leopoldo Sarra. Reinforcement learning with learned gadgets to tackle hard quantum problems on real hardware. *arXiv preprint arXiv:2411.00230*, 2024.
- [31] Xudong Lu, Kaisen Pan, Ge Yan, Jiaming Shan, Wenjie Wu, and Junchi Yan. Qas-bench: rethinking quantum architecture search and a benchmark. In *International conference on machine learning*, pages 22880–22898. PMLR, 2023.
- [32] Chris Ying, Aaron Klein, Eric Christiansen, Esteban Real, Kevin Murphy, and Frank Hutter. Nas-bench-101: Towards reproducible neural architecture search. In *International conference on machine learning*, pages 7105–7114. PMLR, 2019.
- [33] Xuanyi Dong and Yi Yang. Nas-bench-201: Extending the scope of reproducible neural architecture search. *arXiv preprint arXiv:2001.00326*, 2020.
- [34] Nikita Klyuchnikov, Ilya Trofimov, Ekaterina Artemova, Mikhail Salnikov, Maxim Fedorov, Alexander Filippov, and Evgeny Burnaev. Nas-bench-nlp: neural architecture search benchmark for natural language processing. *IEEE Access*, 10:45736–45747, 2022.

- [35] Yash Mehta, Colin White, Arber Zela, Arjun Krishnakumar, Guri Zabergja, Shakiba Moradian, Mahmoud Safari, Kaicheng Yu, and Frank Hutter. Nas-bench-suite: Nas evaluation is (now) surprisingly easy. *arXiv preprint arXiv:2201.13396*, 2022.
- [36] Roger A Horn and Charles R Johnson. *Matrix analysis*. Cambridge university press, 2012.
- [37] Michael A Nielsen and Isaac L Chuang. *Quantum computation and quantum information*. Cambridge university press, 2010.
- [38] Steven R White. Density matrix formulation for quantum renormalization groups. *Physical review letters*, 69(19):2863, 1992.
- [39] Ulrich Schollwöck. The density-matrix renormalization group in the age of matrix product states. *Annals of physics*, 326(1):96–192, 2011.
- [40] Michael JD Powell. A direct search optimization method that models the objective and constraint functions by linear interpolation. In *Advances in optimization and numerical analysis*, pages 51–67. Springer, 1994.
- [41] Mateusz Ostaszewski, Edward Grant, and Marcello Benedetti. Structure optimization for parameterized quantum circuits. *Quantum*, 5:391, 2021.
- [42] Hado Van Hasselt, Arthur Guez, and David Silver. Deep reinforcement learning with double q-learning. In *Proceedings of the AAAI conference on artificial intelligence*, volume 30, 2016.
- [43] Ronald J Williams. Simple statistical gradient-following algorithms for connectionist reinforcement learning. *Machine learning*, 8(3):229–256, 1992.
- [44] Yunseong Nam, Neil J Ross, Yuan Su, Andrew M Childs, and Dmitri Maslov. Automated optimization of large quantum circuits with continuous parameters. *npj Quantum Information*, 4(1):23, 2018.
- [45] Sukin Sim, Peter D Johnson, and Alán Aspuru-Guzik. Expressibility and entangling capability of parameterized quantum circuits for hybrid quantum-classical algorithms. *Advanced Quantum Technologies*, 2(12):1900070, 2019.

A Method Implementation Details

For fair comparison, all methods operate over a unified gate basis $\{RX, RY, RZ, CNOT\}$ and a shared depth budget D . Candidate circuits are allowed to terminate before D through

CRLQAS [9]. CRLQAS formulates QAS as a Markov decision process in which a DQN [42] agent sequentially inserts gates into a growing circuit. The step reward is defined as

$$r_t = \begin{cases} +5 & \text{if } E_t < \xi_t \\ -5 & \text{if } t = L - 1 \text{ and } E_t \geq \xi_t \\ \text{clip}\left(\frac{E_{t-1} - E_t}{|E_{t-1} - E_{\min}| + \epsilon}, -1, 1\right) & \text{otherwise,} \end{cases} \quad (4)$$

where ξ_t is an acceptance threshold that is either progressively tightened via a moving curriculum or held fixed, depending on the task. The policy is trained with n -step DQN ($n = 6$) and an experience replay buffer. Episodes terminate upon reaching the acceptance threshold or the maximum depth D . The gate set matches the benchmark standard with no adaptation required.

HyRLQAS [10]. HYRLQAS extends discrete-action QAS by predicting initial rotation angles alongside gate placement, providing warm-start initializations for the external optimizer rather than replacing it. A refinement mechanism further updates previously assigned angles after each gate insertion. The policy is trained with REINFORCE [43]. The gate set requires no adaptation. Episodes terminate upon reaching the acceptance threshold or maximum depth D , following the same curriculum structure as CRLQAS.

QuantumDARTS [12]. QUANTUMDARTS maintains continuous architecture weights over $\{Rz-Ry-Rz, I, CNOT\}$ and optimizes them jointly with gate parameters via Gumbel-softmax relaxation. Architecture weights are updated only during the search phase; after discretization, the exported circuit undergoes fixed-structure parameter re-optimization using the shared local optimizer. The search and evaluation spaces differ by design: identity slots allow circuits to terminate before D , and each Rz-Ry-Rz block is lowered to primitive $\{RZ, RY, RZ\}$ at evaluation time.

TFQAS [18]. TFQAS applies a three-stage progressive filtering pipeline. Stage 1 ranks S sampled circuits by DAG path count [44]; Stage 2 re-scores the top- R by expressibility [45]; Stage 3 applies the shared local optimizer to the top- K circuits. Gate count is sampled uniformly from $[1, D]$, enabling natural early termination. The original entangler set $\{XX, YY, ZZ\}$ is replaced with CNOT at search time.

GQEQAS [11]. GQEQAS trains an autoregressive transformer online: at each epoch it generates circuits, evaluates them via VQE, and updates with an energy-weighted gradient. Sequence length is sampled uniformly up to the depth budget, allowing early termination. Final energies are reported after parameter re-optimization using the shared local optimizer. The original operator pool is replaced with a discretized token pool over $\{RX, RY, RZ, CNOT\}$.

B Optimizer Parallelization and Execution Backend

Motivation. Circuit-level parameter optimization is the primary computational bottleneck in HAMQASBENCH. For a fixed circuit structure, an external optimizer must repeatedly query the circuit energy until convergence, and as qubit count increases each energy query becomes substantially more expensive. GPU-based state-vector simulation can accelerate individual queries, but its benefit is limited when the optimizer issues strictly sequential calls. Our design therefore targets optimizer structures that admit grouped evaluation and make better use of GPU throughput.

Rotosolve as the scalable optimizer. Rotosolve is well matched to this setting. Each sweep over the active rotation parameters evaluates a fixed three-point probe set $\{0, \pi/2, \pi\}$ per parameter and updates it analytically. With `rotosolve_sweeps=2`, two complete sweeps are performed per optimization call. Because all probe angles within a sweep are known in advance, the corresponding energy queries are assembled into a single batched evaluation rather than launched sequentially.

This exposes two levels of parallelism: probe circuits within a sweep are evaluated together via a batched state-vector backend, and $k = 10$ optimization environments are overlapped across CUDA streams. COBYLA, by contrast, issues adaptive sequential queries (maximum `global_iters`= 100 iterations) and exposes little coarse-grained parallelism, which is why it is retained only for small systems (≤ 6 qubits) where runtime remains manageable.

Empirical efficiency. Table 7 reports wall-clock time per training episode on the BeH2 basis-set ladder using a representative CRLQAS workload. GPU* Rotosolve with $k = 10$ parallel environments reduces per-episode cost to 14.7–27.0 seconds across the 8q–14q range, compared to 195.7–338.0 seconds for CPU Rotosolve, enabling practical benchmarking at scales that would otherwise be infeasible.

Table 7: Wall-clock time per training episode (seconds) on a representative CRLQAS workload over the BeH2 basis-set ladder. GPU* denotes grouped GPU execution with $k = 10$ parallel environments.

Hardware	Optimizer	8q	10q	12q	14q
CPU	COBYLA	48.9	146.7	270.9	429.9
	Rotosolve	42.7	144.9	195.7	338.0
	AdamSPSA	69.7	218.4	439.1	934.2
	PSRAdam	54.5	206.4	243.4	443.0
GPU	COBYLA	—	—	—	—
	Rotosolve	19.0	16.2	21.1	63.2
	AdamSPSA	95.6	98.3	110.9	218.8
	PSRAdam	45.2	55.8	69.2	131.1
GPU*	COBYLA	—	—	—	—
	Rotosolve	14.7	12.9	13.4	27.0
	AdamSPSA	79.0	70.7	81.3	104.2
	PSRAdam	40.9	48.7	48.4	69.8

C Training Hyperparameters and Compute Budget

Per-method training configuration. Table 8 lists the key hyperparameters for each method. For RL methods (CRLQAS, HYRLQAS), one episode denotes a complete circuit-construction trajectory of at most D gate insertions, with 8 environments rolled out in parallel. The two methods share the same overall configuration except for batch size: CRLQAS uses a larger replay buffer update (batch size 1000) while HYRLQAS uses batch size 16 consistent with its REINFORCE update rule. Both use 8000 episodes for simpler molecules and 15000 for larger or more challenging instances. For QUANTUMDARTS, the search phase runs for n_{epochs} with $n_{\text{inner}} = 10$ gradient steps per epoch; architecture weights are updated only during this search phase, after which the best discrete circuit undergoes fixed-structure parameter re-optimization with COBYLA or Rotosolve. The configured post-search budget and learning rates vary by problem size as shown in Table 8, but architecture parameters are not updated post-search. For TFQAS, no gradient updates are performed; the budget is expressed as the number of candidate circuits sampled. For GQEQAS, one epoch draws `online_sample_count`= 250 circuits from the current generative model, evaluates them via VQE, and updates the transformer with the resulting energy-weighted objective; 1000 epochs are used for simpler molecules and 1500 for larger instances.

Table 8: Key training hyperparameters per method. D denotes maximum circuit depth (Shallow: $D = 10$; Deep: $D = 50$). VQE optimizer: COBYLA (`global_iters`= 100) for $\leq 6q$; Rotosolve (`sweeps`= 2) for $> 6q$. Episodes listed as easy/hard split by molecule complexity.

Method	Training unit	Budget	Depth D	Policy update	Batch size
CRLQAS	episode ($\times 8$ envs)	8k / 15k ep	10 / 50	DQN (n -step, $n = 6$)	1000
HyRLQAS	episode ($\times 8$ envs)	8k / 15k ep	10 / 50	REINFORCE	16
QuantumDARTS	epoch ($n_{\text{inner}} = 10$)	500–900 ep	10 / 50	Adam ($\theta: 10^{-2}$ – 5×10^{-3} , $\alpha: 5 \times 10^{-3}$ – 3×10^{-3})	—
TFQAS	candidate circuits	$S = 11k$ – $23k$	10 / 50	None	—
GQEQAS	epoch (online refresh)	1k / 1.5k ep	10 / 50	Adam	—

Table 9: Molecule generation parameters for HAMQASBENCH.

Tier	Molecule	Geometry (Å)	Charge	Basis	CAS(n_e, n_o)	Frozen e^-	n_q
1	BeH2_STO3G	Be(0,0,0); H(0,0,1.326); H(0,0,-1.326)	0	STO-3G	(2e, 3o)	4	6
1	LiH_Equil	Li(0,0,0); H(0,0,1.595)	0	STO-3G	(2e, 3o)	2	6
2	CH2	C(0,0,0); H(0,0.86,0.73); H(0,-0.86,0.73)	0	STO-3G	(2e, 4o)	6	8
3	H2_Stretch	H(0,0,0); H(0,0,2.500)	0	STO-3G	(2e, 2o)	0	4
3	H2O_StrongCorr	O(0,0,0); H(0,1.186,0.918); H(0,-1.186,0.918)	0	STO-3G	(4e, 4o)	6	8
3	H4_Chain	H(0,0,0); H(0,0,1); H(0,0,2); H(0,0,3)	0	STO-3G	(4e, 4o)	0	8
4	H3_Linear [‡]	H(0,0,0); H(0,0,1); H(0,0,2)	1	STO-3G	(2e, 3o)	0	6
5	BeH2_631G	Be(0,0,0); H(0,0,1.326); H(0,0,-1.326)	0	6-31G	(2e, 4o)	4	8
5	BeH2_6311G	Be(0,0,0); H(0,0,1.326); H(0,0,-1.326)	0	6-311G	(2e, 5o)	4	10
5	BeH2_CCPVDZ	Be(0,0,0); H(0,0,1.326); H(0,0,-1.326)	0	cc-pVDZ	(2e, 6o)	4	12
5	BeH2_CCPVDZ	Be(0,0,0); H(0,0,1.326); H(0,0,-1.326)	0	cc-pVDZ	(4e, 7o)	2	14

[‡] H_3^+ cation; Tier 4 uses nearest-neighbour connectivity.

Evaluation during training. For all learning-based methods, periodic evaluation is performed every e_{eval} episodes by sampling $K_{\text{eval}} = 50$ circuits from the current model without gradient updates. The best circuit found across all evaluation checkpoints—measured jointly by energy error and CNOT count—is retained as the method’s final result. For TFQAS, evaluation is applied once after the top- $K = 50$ circuits undergo final VQE parameter optimization.

Training budget alignment. Comparing training budgets across paradigms is non-trivial because one episode incurs fundamentally different computational costs depending on the method: an RL episode involves D sequential VQE calls during trajectory rollout, whereas one QUANTUMDARTS epoch processes all circuit slots simultaneously via a single backward pass. We adopt episode/epoch count as the primary budget axis and report wall-clock time per episode in Appendix B to allow cost-adjusted comparisons.

D Molecule Generation and Hamiltonian Construction

Table 9 lists the generation parameters for all molecules in HAMQASBENCH. For each instance, we provide the molecular geometry, basis set, active space configuration (CAS), and the resulting number of qubits. All geometries are specified in Angstrom (Å). Electronic structure calculations use a singlet reference (mult = 1) unless otherwise noted. Frozen electrons are defined as the difference between the total and active electrons.

Implementation details. Hamiltonians are generated using a standard quantum chemistry pipeline. We first perform mean-field calculations to obtain molecular orbitals, followed by active-space selection to define the CAS(n_e, n_o) configuration. The resulting fermionic Hamiltonian is mapped to qubits via the Jordan–Wigner transformation. All instances use consistent numerical settings and deterministic workflows.

Reproducibility. All Hamiltonians can be deterministically reconstructed from the parameters in Table 9, with no stochastic procedures involved, and are directly compatible with standard libraries such as PennyLane.

E Hamiltonian Fingerprint Theory

The field of quantum chemistry has historically analysed structural properties and, in particular, approximate solutions of the full configuration interaction (FCI) Hamiltonian to diagnose the complexity of the system. The structure of the FCI Hamiltonian exhibits, in overwhelming number of cases, sparsity with known couplings by excitation rank; high symmetry based on well established spin multiplicity and spatial group theory concepts; and diagonal dominance due to large contributions from mean-field terms compared to off-diagonal coupling. This has allowed the proliferation of classically computationally efficient methods that work in the majority of cases such as coupled

cluster theory or truncated configuration interaction. Similarly, it has led to problem specific ansatz design for VQE on these problems such as the UCCSD ansatz used in the initial formulation of VQE. In particular, many existing theories and ansatz work well for problems described well by a single-reference Slater determinant which allows them to centre around the Hartree-Fock solution and its excitations.

However, it is well known that these theories and assumptions break down for larger, strongly correlated materials that we wish to study such as: open-shell systems, bond breaking, transition-metal complexes, and large biological systems which often require multi-reference solutions with complicated entanglement structure. We therefore aim to treat the common assumptions on the CI Hamiltonian instead as metrics to characterise the difficulty of the electronic structure problem and identify useful Hamiltonians for use as benchmarking.

E.1 Operator and Computational basis Fingerprints

As an example, iterative diagonalisation procedures commonly rely on the Hamiltonian being diagonally dominant. Consider a Hamiltonian H with matrix elements $h_{i,j}$. Diagonal dominance is defined as:

$$|h_{i,i}| \geq \sum_{i \neq j} |h_{i,j}|. \quad (5)$$

This is well justified using Gershgorin's circle theorem, illustrated in Figure 1b) in the main text, which says that every eigenvalue of H lies within at least one of the Gershgorin discs which are discs centered at $h_{i,i}$ with radius $\sum_{i \neq j} |h_{i,j}|$. When the matrix is diagonally dominant, the circles are narrow and may become disjoint. If a disc or set of discs become isolated, then they will contain as many eigenvalues as they have discs, with each eigenvalue well bounded around the corresponding matrix element. Overlapping discs reflect strong off-diagonal coupling in the computational basis and can indicate multi-reference character and cause simple ansatz and classically efficient methods to lose accuracy.

We propose three related metrics to measure how a given Hamiltonian violates this property. The first is a direct measure of overall diagonal dominance in the Pauli operator basis. The remaining two are defined in the matrix representation in the computational basis: assuming diagonal dominance has been violated overall, they measure the fraction of rows that remain diagonally dominant and the value of the weakest diagonally dominant row.

We will now derive the metrics based on the definition of diagonal dominance. We start with a Hamiltonian in the Pauli operator basis:

$$H = \sum_i c_i P_i,$$

where P_i are Pauli strings and c_i are their coefficients, we can write the matrix elements as an expectation value:

$$h_{i,j} = \langle i | H | j \rangle = \sum_k c_k \langle i | P_k | j \rangle. \quad (6)$$

Now, for diagonal entries, the only contributions will be from P_i that have I and Z qubit components which will contribute either 1 or -1 . We can therefore write:

$$h_{i,i} = \sum_{k \in \{I, Z\}} c_k a_{i,k}, \quad (7)$$

where $a_{i,k}$ is either 1 or -1 and is determined by how many Z in the Pauli string coincide with a qubit with state 1 in $|i\rangle$.

To consider strings with X and Y , consider enumerating the state into n qubits i.e. $|i\rangle = |q_0 q_1 \dots q_b \dots q_{n-1}\rangle$ with some index b . A Pauli string, P_k that has any X or Y at some qubit index b will flip q_b from 0 to 1 or vice versa. This means that any qubit string containing X or Y will not contribute to the diagonal component.

For off-diagonals, strings containing only Z and I will not contribute as they cannot transform computational basis states. P_k with X and Y strings will only contribute when $|i\rangle$ is related to $|j\rangle$

by flipping the qubits with X or Y terms. Since a single Pauli string cannot create a superposition between computational basis states, it will only map one basis state to another basis state, so, for each row i , for each Pauli P_k , there will be only one non-zero j . Therefore, we can immediately treat the sum over the row, since each Pauli will only contribute to one element in the row:

$$\sum_j h_{i,j} = \sum_{k \in \{X,Y\}} c_k b_{i,k}, \quad (8)$$

where $b_{i,k} \in \{1, -1, i, -i\}$. Overall, we have diagonal dominance forming the following chain of inequalities:

$$\left| \sum_k c_k b_{i,k} \right| \leq \sum_j |h_{i,j}| \leq |h_{ii}| = \left| \sum_k c_k a_k \right| \leq \sum_k |c_k|, \quad (9)$$

where we have used the triangle inequality for the last step. Note that this upper bound works for all rows, where the original diagonal dominance condition was only for each row. While this statement is true and can be evaluated to determine diagonal dominance, we also investigate a stronger statement. We can form an upper bound for the off-diagonals using the triangle inequality:

$$\sum_j |h_{i,j}| \leq \sum_{k \in \{X,Y\}} |c_k|, \quad (10)$$

which gives us a sufficient but not necessary condition for diagonal dominance:

$$\sum_{k \notin \{I,Z\}} |c_k| \leq \sum_{k \in \{I,Z\}} |c_k|. \quad (11)$$

We want to define an overall metric that can be a proxy for how difficult it is to find the ground state. We can use the fraction of the Pauli coefficients that contribute to the diagonal as a ratio of overall contribution:

$$r_Z = \frac{\sum_{P_i \in Z\text{-only}} |c_i|}{\sum_i |c_i|}, \quad (12)$$

where as $r_Z > 0.5$, the more diagonally dominant the Hamiltonian will be. We note that this is a metric independent of row, distinct from our computational metrics G_1 and G_2 which measure the proportion of rows and the weakest diagonal dominance row respectively.

E.2 Multiqubit interaction metric

Similarly, we take inspiration from results in quantum computational complexity theory. In complexity theory, the k -local Hamiltonian problem is QMA-complete. k -local refers to each Pauli string in the Hamiltonian having at most " k " non-identity terms i.e. only acting on " k " qubits at a time. In particular, it is well known that 2-local Hamiltonians can have ground states with long range non-trivial quantum correlations, the typical example being a 2D antiferromagnetic Heisenberg model and, similarly, it is why we can achieve universal gate sets for quantum computing with only two-qubit entangling gates.

As a comparison, 1-local Hamiltonians are trivial to find the ground state and are in P regardless of the number of qubits. To that end, we define a metric to determine the weight of the entangling terms, which cause the problem to be QMA-complete. Similarly, this also measures how badly the ground state can be approximated by the trivial 1-local component of the Hamiltonian.

E.3 Energy Metrics

The energy gap is a common metric for measuring difficulty of finding a ground state and is tied to degeneracy. Firstly, many ground state theorems are only applicable to gapped Hamiltonians. Secondly, for this work, we consider an energy gap of zero as equivalent to having degenerate ground states. Typically in chemistry, for degenerate ground states such as triplet states, the energy gap will be defined to the next highest triplet state or something similar. Indeed, the degeneracy due to spin multiplicity and spatial symmetry is well known and can be readily predicted. For

Algorithm 1 Critical-Structure Extraction

Require: Snapshot records \mathcal{S} , bucket width w , selected bucket b , beam width B , branching factor k , prune budget M , bucket slack δ_{bucket} , reconstruction slack δ_{rec} , per-step tolerance τ

Ensure: Retained circuits $\{C_{\text{ret}}\}$ and cross-snapshot structure summaries

- 1: Bucket snapshot events by quantized error; select records \mathcal{S}_b in bucket b
- 2: Identify anchor signatures \mathcal{A} from frequent gate-qubit signatures in \mathcal{S}_b
- 3: Sample representative subset $\tilde{\mathcal{S}}_b \subseteq \mathcal{S}_b$, balanced across runs
- 4: **for** each snapshot $s \in \tilde{\mathcal{S}}_b$ **do**
- 5: Reconstruct circuit C and re-optimize parameters to obtain baseline $C^{(0)}$ with error $\varepsilon(C^{(0)})$
- 6: Set $\varepsilon_{\text{allow}} = \max(b + \delta_{\text{bucket}}, \varepsilon(C^{(0)}) + \delta_{\text{rec}})$
- 7: **for** each gate $g_j \in C^{(0)}$ **do**
- 8: Remove g_j , re-optimize from warm start, compute $\Delta_e(j) = \varepsilon(C^{(0)} \setminus g_j) - \varepsilon(C^{(0)})$
- 9: **end for**
- 10: Construct deletion prior $\pi(j)$ from $\{\Delta_e(j)\}$; gates in \mathcal{A} receive reduced deletion probability
- 11: Initialize $\mathcal{B}_0 = \{C^{(0)}\}$, evaluation counter $m \leftarrow |C^{(0)}|$
- 12: **for** $t = 0, 1, \dots$ until no feasible expansion or $m \geq M$ **do**
- 13: $\mathcal{B}_{t+1} \leftarrow \emptyset$
- 14: **for** each $C \in \mathcal{B}_t$ **do**
- 15: Sample k gates according to deletion prior $\pi(j)$
- 16: **for** each sampled gate g_j **do**
- 17: $C' \leftarrow C \setminus g_j$; re-optimize from warm start; $m \leftarrow m + 1$
- 18: **if** $\varepsilon(C') \leq \varepsilon_{\text{allow}}$ **and** $|\varepsilon(C') - \varepsilon(C)| \leq \tau$ **then**
- 19: Add C' to \mathcal{B}_{t+1}
- 20: **end if**
- 21: **end for**
- 22: **end for**
- 23: Deduplicate \mathcal{B}_{t+1} by gate sequence; retain top B ranked by $(|C|, \varepsilon(C), \Delta_{\text{total}})$
- 24: **end for**
- 25: $C_{\text{ret}} \leftarrow$ smallest feasible circuit encountered
- 26: **end for**
- 27: Aggregate retained structures across snapshots

our Hamiltonians, it is possible to remove degeneracy by restricting the Hilbert space to a specific spin/charge/symmetry sector, however we use degeneracy to create gapless Hamiltonians to serve as a challenge for architecture search algorithms, which can demonstrate its scaling when tackling real world problems with degeneracy that cannot be predicted or removed.

E.4 Ground state Metrics

Measuring multipartite entanglement structure is highly non-trivial and multiple competing metrics exist. Fortunately, bipartite entanglement metrics are well understood and, therefore, we propose to use the Von Neumann Entropy from separating one qubit from the ground state for each qubit. While this metric requires access to the exact ground state, it is common in quantum chemistry to calculate similar information theoretic quantities using approximations of the ground state. For instance, for larger benchmarks, we can use the 1-RDM, 2-RDM, or even a Matrix Product State approximation of the ground state which are able to be calculated with classical computers.

F Critical-Structure Extraction Details

Algorithm 1 formalizes the critical-structure extraction procedure. Given low-error training snapshots from a fixed molecule–method setting, the procedure combines counterfactual gate ablation with constrained beam pruning under an explicit error budget, returning compact retained circuits and cross-snapshot structure summaries.

Snapshot collection and bucketing. Snapshots $(C_i, \theta_i, \varepsilon_i)$ are grouped into quantized error buckets and analysis is restricted to a selected bucket, ensuring circuits are compared at a consistent

performance level. Representative snapshots are sampled with bias toward late training and balanced across random seeds to avoid dominance by a single run.

Circuit reconstruction and baseline optimization. Each snapshot is reconstructed into a gate-level circuit and parameters are re-optimized to obtain a stable baseline $C^{(0)}$, accommodating minor discrepancies between stored traces and locally optimized circuits.

Counterfactual gate importance. For each gate $g_j \in C^{(0)}$, we remove it and re-optimize the remaining circuit from a warm start (inheriting current parameter values), computing $\Delta_e(j) = \varepsilon(C^{(0)} \setminus g_j) - \varepsilon(C^{(0)})$. Using warm-start re-optimization ensures that $\Delta_e(j)$ reflects the true structural contribution of g_j rather than a parameter initialization artifact.

Constrained beam pruning. From the baseline importance scores, we construct a deletion prior $\pi(j)$ inversely weighted by $\Delta_e(j)$, so that gates with smaller degradation are more likely to be sampled for removal. Gates matching frequent gate-qubit signatures across snapshots (anchor gates) receive reduced deletion probability to protect structurally recurring motifs. At each pruning step, k gates are sampled per candidate according to $\pi(j)$ —the prior is fixed from the baseline and not recomputed as the circuit shrinks. A candidate is retained only if it satisfies both the error tolerance $\varepsilon_{\text{allow}}$ and the per-step degradation bound τ . The beam retains the top B candidates ranked by gate count, energy error, and cumulative error degradation Δ_{total} .

Outputs. For each snapshot, the procedure returns the smallest retained circuit C_{ret} and records its redundancy ratio $\rho = (|C^{(0)}| - |C_{\text{ret}}|)/|C^{(0)}|$. Across snapshots, retained gate-qubit signatures are aggregated to identify common structural motifs.

G More Experiment Results

G.1 Training-stage Results and Eval Gap

Table 10 reports the best circuits discovered during training for each method–molecule pair. Comparing against the evaluation-stage results in Table 3, two patterns emerge.

First, for Tier 1 and the small-scale Tier 3 instance `H2_Stretch`, the training–eval gap is negligible: methods that find chemical-accuracy solutions during training reliably reproduce them at evaluation, indicating stable policy convergence in simple and well-conditioned regimes.

Second, the gap widens substantially in more challenging settings. On `T2_CH2`, RL-based methods discover near-exact solutions during training (CRLQAS, HYRLQAS, GQEQAS all reach errors below 10^{-6} mHa) but fail to reproduce them consistently at evaluation, reflecting the eigenstate commitment and policy instability described in Section 5. On Tier 3 larger instances and Tier 4, training-stage errors are systematically lower than eval-stage errors across all methods, suggesting that low-error circuits are discovered sporadically during exploration but do not correspond to stable learned policies. TFQAS shows no training–eval gap by construction, as it is training-free and produces a single ranked set of candidates.

G.2 Tier 1 Full Gate Statistics

Table 12 reports the complete gate statistics for all chemical-accuracy circuits discovered during training in Tier 1, covering both `BeH2_ST03G` and `LiH_Equi1` across all methods and budget settings. Across both molecules, HYRLQAS consistently achieves the lowest redundancy rates (6.7% shallow and 25.3% deep on `BeH2_ST03G`; 34.9% on `LiH_Equi1`), indicating that its hybrid action space effectively suppresses unnecessary gate placement even when a larger budget is available. All other methods show substantially higher redundancy, with QUANTUMDARTS exceeding 92% across all settings.

Table 10: Best Training-stage QAS results on the T1–T4 diagnostic tiers of HAMQASBENCH.

Molecule	T1_BeH2_6q (Shallow)			T1_BeH2_6q (Depth)			T1_LiH_Equil_6q (Shallow)			T1_LiH_Equil_6q (Depth)			T2_CH2_8q		
	Error	Cnot	Rot	Error	Cnot	Rot	Error	Cnot	Rot	Error	Cnot	Rot	Error	Cnot	Rot
CRLQAS	2.68E-04	4	5	2.68E-04	5	4	6.03E-04	5	5	2.34E-04	18	10	6.19E-07	8	6
HyRLQAS	5.54E-04	3	3	2.56E-04	21	11	1.05E-03	0	5	2.47E-04	12	7	6.19E-07	11	5
QuantumDARTS	5.54E-04	11	6	6.69E-05	90	48	1.05E-03	3	3	1.05E-03	3	3	5.66E-03	66	22
GQEQAS	5.54E-04	0	2	5.54E-04	0	3	1.05E-03	8	8	1.05E-03	4	19	6.20E-07	10	17
TFQAS	5.54E-04	5	4	1.89E-02	26	23	1.05E-03	5	4	1.01E-02	24	21	3.69E-01	35	26

Molecule	T3_H2_Stretch_4q			T3_H2O_StrongCorr_8q			T3_H4_Chain_8q			T4_H3_Linear_6q_All			T4_H3_Linear_6q_Linear		
	Error	Cnot	Rot	Error	Cnot	Rot	Error	Cnot	Rot	Error	Cnot	Rot	Error	Cnot	Rot
CRLQAS	4.44E-11	8	4	5.87E-03	34	25	3.38E-02	39	12	1.36E-03	25	19	1.69E-02	26	19
HyRLQAS	1.41E-07	13	7	6.46E-03	26	12	3.98E-02	16	11	9.36E-03	27	11	2.35E-02	9	7
QuantumDARTS	2.44E-03	24	12	1.43E-01	13	6	6.78E-02	13	9	4.64E-02	44	9	4.64E-02	19	6
GQEQAS	4.39E-05	4	12	4.67E-02	0	6	6.69E-02	7	24	2.35E-02	7	8	4.64E-02	3	12
TFQAS	4.71E-03	28	19	2.91E-01	37	32	7.80E-01	40	29	1.71E-01	24	24	2.17E-01	24	24

Table 11: Best Training-stage QAS results on the T5 same-family BeH₂ scaling ladder of HAMQASBENCH.

Molecule	T5_BeH2_6q			T5_BeH2_631G_8q			T5_BeH2_631G_10q			T5_BeH2_CCPVDZ_12q			T5_BeH2_CCPVDZ_14q		
	Error	Cnot	Rot	Error	Cnot	Rot	Error	Cnot	Rot	Error	Cnot	Rot	Error	Cnot	Rot
CRLQAS	2.68E-04	4	5	1.15E-04	42	10	2.48E-04	35	10	1.24E-03	46	17	5.01E-03	18	9
HyRLQAS	5.54E-04	3	3	2.34E-04	18	9	2.48E-04	13	6	1.24E-03	42	32	5.68E-03	33	6
QuantumDARTS	5.54E-04	11	6	2.17E-03	1	6	8.97E-04	1	6	2.60E-01	19	3	3.01E-01	114	12
GQEQAS	5.54E-04	0	2	2.17E-03	7	21	8.96E-04	6	12	1.87E-03	8	11	6.15E-03	0	9
TFQAS	5.54E-04	5	4	2.07E-01	36	31	3.83E-01	51	41	1.45E-01	50	29	3.26E-01	45	32

G.3 Topology Analysis: H₄ Chain Connectivity Comparison

To isolate the effect of connectivity constraints on entanglement structure encoding—independent of the eigenstate ambiguity present in the degenerate H3_Linear instance—we apply per-qubit entropy analysis to H4_Chain under two connectivity settings: all-to-all and nearest-neighbour linear.

Table 13 shows that enforcing linear connectivity increases MAE_S from 0.068 to 0.121 while also worsening energy error from 33.55 to 48.03 mHa. The per-qubit breakdown in Table 14 reveals the structural mechanism underlying this degradation.

Under all-to-all connectivity, the pruned circuit captures interior qubit entanglement (q_2 – q_5) reasonably well but fails on boundary qubits q_1 and q_6 (circuit $S = 0$ vs. exact ≈ 0.12). Under linear connectivity, this failure extends to all four boundary qubits (q_0, q_1, q_6, q_7), with \bar{S}_{circuit} dropping from 0.130 to 0.077. Critically, the linear-connectivity circuit achieves higher energy error despite encoding less entanglement structure, confirming the decoupling between energy and structural fidelity identified in Section 5: a circuit can find a lower-energy solution in a restricted topology by concentrating gates on interior qubits, while systematically failing to represent the boundary correlations required by the Hamiltonian. This demonstrates that connectivity constraints impose a structural bottleneck that energy metrics alone cannot detect.

G.4 Tier 5 Full Scalability Results

Table 15 reports training-stage and evaluation-stage results for all methods across the BeH₂ basis ladder. Three observations sharpen the main-text analysis.

10-qubit as the key inflection point. At 10 qubits (BeH₂_6311G), methods stratify into three tiers: HYRLQAS achieves 100% evaluation success rate with a mean of 1.0 CNOT per chemical-accuracy circuit, CRLQAS achieves 90% with a mean of 4.5 CNOTs, QUANTUMDARTS succeeds sporadically (15%), and GQEQAS and TFQAS fail entirely. The low CNOT counts for both RL methods confirm that they correctly exploit the near-product ground-state structure ($S_{\text{max}} = 0.011$) at this scale.

Table 12: Full gate statistics for chemical-accuracy circuits in Tier 1. Mean and standard deviation of rotation-gate count (Rot), CNOT count, and total gate count are reported across all circuits within chemical accuracy. — indicates no chemical-accuracy circuits were found under that budget.

<i>BeH₂ STO-3G</i>							
Method	Budget	Rot mean	Rot std	CNOT mean	CNOT std	Total mean	Redundancy
CRLQAS	shallow	3.17	1.22	2.72	1.77	5.89	66.1%
HyRLQAS	shallow	2.06	0.39	0.08	0.52	2.14	6.7%
GQEQAS	shallow	7.78	1.70	0.14	0.34	7.92	74.7%
TFQAS	shallow	4.39	0.70	5.45	0.62	9.85	79.7%
QuantumDARTS	shallow	9.60	3.10	29.20	17.38	38.80	94.8%
CRLQAS	deep	4.45	3.17	5.65	6.00	10.10	80.2%
HyRLQAS	deep	2.21	1.08	0.47	2.45	2.68	25.3%
GQEQAS	deep	11.79	4.54	1.75	3.48	13.54	85.2%
TFQAS	deep	—	—	—	—	—	—
QuantumDARTS	deep	9.60	3.84	22.75	13.88	32.35	93.8%
<i>LiH (equil.)</i>							
Method	Budget	Rot mean	Rot std	CNOT mean	CNOT std	Total mean	Redundancy
CRLQAS	shallow	3.06	1.22	2.88	1.76	5.94	66.3%
HyRLQAS	shallow	2.02	0.36	0.11	0.59	2.13	6.1%
GQEQAS	shallow	7.44	2.47	0.07	0.37	7.51	73.4%
TFQAS	shallow	4.11	0.70	5.48	0.58	9.59	79.2%
CRLQAS	deep	4.97	3.69	6.47	6.73	11.43	82.5%
HyRLQAS	deep	2.34	1.46	0.73	3.16	3.07	34.9%
QuantumDARTS	deep	8.80	3.96	16.70	14.99	25.50	92.2%
GQEQAS	deep	9.81	6.37	6.36	7.43	16.17	87.6%
TFQAS	deep	—	—	—	—	—	—

Table 13: Entanglement structure consistency for H4_Chain under two connectivity settings. MAE_S measures deviation from the exact ground-state per-qubit entropy profile.

Connectivity	Error (mHa)	\bar{S}_{exact}	\bar{S}_{circuit}	MAE_S
All-to-all	33.55	0.198	0.130	0.068
Linear	48.03	0.198	0.077	0.121

12-qubit: solutions exist but cannot stabilize. At 12 qubits (BeH₂_CCPVDZ), CRLQAS discovers circuits reaching 1.24 mHa during training (below chemical accuracy) with a training success rate of 0.1%, but evaluation success rate drops to 0%. Critical-structure extraction confirms that 6 such circuits exist in the training trajectory; their gate counts range from 8 to 64 with redundancy rates of 25–78%, indicating that the policy remains in an exploratory regime and has not converged to a compact reusable structure.

14-qubit: complete failure across all methods. At 14 qubits, no method achieves chemical accuracy at either training or evaluation stage. CRLQAS produces the lowest evaluation error (6.15 mHa), still more than four times above the chemical accuracy threshold. The exponential growth of the search space ($2^{14} = 16,384$ dimensions) appears to be the dominant bottleneck, consistent with the controlled entanglement structure across the ladder.

Entanglement structure is not the bottleneck. Per-qubit entropy analysis across the ladder confirms that ground-state entanglement complexity remains controlled throughout (Table 16). At 10 qubits, solved circuits achieve $MAE_S = 0.001$. At 12 qubits, the 6 near-chemical-accuracy circuits discovered during training all reproduce the same entanglement profile ($MAE_S = 0.005$, $Std = 0.000$) despite gate counts ranging from 8 to 64—the policy has not converged to a compact structure, but when it does find a solution it correctly encodes the quantum state. At 14 qubits, a single training circuit (25 gates, 5.92 mHa) is available for analysis; its $MAE_S = 0.018$ confirms the ground state remains near-product ($S_{\text{max}} = 0.039$). However, critical-structure extraction re-optimization recovers only 328 mHa from this circuit, compared to the training error of 5.92 mHa—the circuit

Table 14: Per-qubit von Neumann entropy $S(q)$ for H4_Chain pruned circuits under all-to-all and linear connectivity, compared against the exact ground state. Values of 0.000 indicate qubits whose entanglement is completely unrepresented by the circuit.

	q_0	q_1	q_2	q_3	q_4	q_5	q_6	q_7
Exact	.124	.124	.274	.274	.284	.284	.109	.109
All-to-all	.062	.000	.213	.245	.245	.213	.000	.062
Linear	.000	.000	.153	.153	.153	.153	.000	.000

Table 15: Training-stage and evaluation-stage results for the BeH2 basis ladder (Tier 5). SR denotes success rate at chemical accuracy (1.6 mHa). — indicates no chemical-accuracy solutions found.

Method	System	Train Best (mHa)	Train SR	Eval Best (mHa)	Eval SR
CRLQAS	8q	1.99	0.0%	0.23	0%
HyRLQAS	8q	0.23	0.1%	2.17	0%
QuantumDARTS	8q	—	—	2.17	0%
GQEQAS	8q	—	—	24.57	0%
TFQAS	8q	—	—	197.39	0%
CRLQAS	10q	0.13	90.2%	0.90	90%
HyRLQAS	10q	0.90	98.7%	0.90	100%
QuantumDARTS	10q	—	—	0.90	15%
GQEQAS	10q	—	—	35.48	0%
TFQAS	10q	—	—	390.42	0%
CRLQAS	12q	1.24	0.1%	2.00	0%
HyRLQAS	12q	2.00	0.0%	—	0%
QuantumDARTS	12q	—	—	2.00	0%
GQEQAS	12q	—	—	269.68	0%
TFQAS	12q	—	—	209.00	0%
CRLQAS	14q	5.15	0.0%	6.15	0%
HyRLQAS	14q	6.15	0.0%	—	0%
QuantumDARTS	14q	—	—	273.00	0%
GQEQAS	14q	—	—	711.00	0%
TFQAS	14q	—	—	6.19	0%

structure is sound but the optimizer fails to recover the correct parameters in the $2^{14} = 16,384$ -dimensional space within the allotted restarts. This reveals a two-layer failure at 14 qubits: the search policy can occasionally discover a structurally correct circuit, but neither the policy nor the optimizer can reliably exploit it. Together, these results confirm that performance degradation across the ladder is driven by search space growth rather than increasing entanglement complexity, directly supporting the Tier 5 design rationale.

Table 16: Per-qubit entropy consistency for the BeH2 basis ladder. At 14q, critical-structure extraction reoptimization recovers 328 mHa from a training circuit with 5.92 mHa error, indicating optimizer failure in the 2^{14} -dimensional parameter space rather than structural failure.

System	n_q	Error (mHa)	\bar{S}_{exact}	\bar{S}_{circuit}	MAE $_S$
BeH ₂ 6-311G	10	0.13	0.005	0.004	0.001
BeH ₂ cc-pVDZ	12	1.24	0.011	0.006	0.005
BeH ₂ cc-pVDZ	14	5.92 [†]	0.020	0.002	0.018

[†] Training-stage error; critical-structure extraction reoptimization baseline = 328 mHa.